Carbon 188 (2022) 229–237

Contents lists available at ScienceDirect

Carbon

journal homepage: www.elsevier.com/locate/carbon

Unraveling the origin of near-infrared emission in carbon dots by ultrafast spectroscopy

Yoonsang Park [a, b, 1], Minh Dao Tran [c, d, 1], Yujin Kim [e], Sungyeon Won [e], Young-Hoon Kim [f, g], Tae-Woo Lee [h], Tom Gregorkiewicz [i], Young Hee Lee [c, d, ***], Ji-Hee Kim [c, d, **], Woosung Kwon [a, e, *]

[a] Institute of Advanced Materials and Systems, Sookmyung Women's University, Seoul, 04310, Republic of Korea
[b] Nano Convergence Technology Research Center, Korea Electronics Technology Institute (KETI), Seongnam, 13509, Republic of Korea
[c] Center for Integrated Nanostructure Physics (CINAP), Institute for Basic Science (IBS), Suwon, 16419, Republic of Korea
[d] Department of Energy Science, Sungkyunkwan University, Suwon, 16419, Republic of Korea
[e] Department of Chemical and Biological Engineering, Sookmyung Women's University, Seoul, 04310, Republic of Korea
[f] Department of Materials Science and Engineering, Seoul National University, Seoul, 08826, Republic of Korea
[g] Department of Energy Engineering, Hanyang University, Seoul, 04763, Republic of Korea
[h] Department of Materials Science and Engineering, School of Chemical and Biological Engineering, Institute of Engineering Research, Research Institute of Advanced Materials, Nano Systems Institute, Seoul National University, Seoul, 08826, Republic of Korea
[i] Van der Waals-Zeeman Institute, University of Amsterdam, Science Park 904, 1098, XH Amsterdam, the Netherlands

ARTICLE INFO

Article history:
Received 21 July 2021
Received in revised form
22 November 2021
Accepted 26 November 2021
Available online 1 December 2021

Keywords:
Carbon dot
Near-infrared
Photoluminescence mechanism
Energy structure
Ultrafast spectroscopy

ABSTRACT

Carbon dots (CDs) are unique light-emissive nanoparticles that are valuable for various applications. However, their complex chemical structures and the limited research interest in their visible-light emission hinder the understanding of their emission structures. Herein, we report the existence of near-infrared (NIR) emissive states originating from the graphitic cores in CDs, which exhibit a completely different behavior from their well-known visible emissive states. Using ultrafast spectroscopy and density functional theory (DFT) calculations, we elucidate the emission mechanism and suggest that small (1–2 nm) graphitic subregions in CDs produce the NIR emissive states, which are rarely affected by surface chemistry changes. Our proposed mechanism and its universality are investigated comprehensively by a comparative analysis with graphene oxide and other types of CDs obtained by different synthetic methods. Finally, we propose a comprehensive emission structure of CDs and redefine the role of structural components in visible-to-NIR emission.

1. Introduction

Carbon dots (CDs) are fluorescent carbonaceous nanoparticles with unique optical properties, exhibiting efficient absorption in the UV range and visible-light photoluminescence (PL) [1–13]. Furthermore, it has been verifiably demonstrated that different photoluminescent emission bands can be induced within a single CD; this is an inherent feature that is not possible with conventional fluorophores such as semiconductor quantum dots [14]. Moreover, the excellent biocompatibility, ease of surface functionalization, electron transfer abilities, and chemical inertness of CDs make them valuable in various fields, including biomedicine, optoelectronics, chemical sensing, photovoltaics, and photocatalysis [15–21].

To date, numerous studies have been conducted to evaluate the optical characteristics of CDs [22–25]. Although their precise structures differ based on the synthesis method, they all exhibit similar visible-light PL. Although the actual mechanism behind this PL is still open to debate, it is well known that this phenomenon is not owing to quantum size effects but because of the localized electronic states formed by surface functional groups, which are

* Corresponding author. Institute of Advanced Materials and Systems, Sookmyung Women's University, Seoul, 04310, South Korea.
** Corresponding author. Department of Energy Science, Department of Energy Science, Sungkyunkwan University, Suwon, 16419, South Korea.
*** Corresponding author. IBS Center for Integrated Nanostructure Physics (CINAP), Institute for Basic Science, Suwon, 16419, South Korea.
E-mail addresses: leeyoung@skku.edu (Y.H. Lee), kimj@skku.edu (J.-H. Kim), wkwon@sookmyung.ac.kr (W. Kwon).
[1] These authors contributed equally to this work.

https://doi.org/10.1016/j.carbon.2021.11.063
0008-6223/

termed as "surface states." [22,26–30] On the other hand, recent studies have reported the phenomena of CDs exhibiting unexpected long-wavelength PL or even near-infrared (NIR) PL and have generated tremendous interest in the NIR PL characteristics of CDs [6,31–40]. However, most of the existing studies on PL in CDs have focused only on the mechanism of visible PL, particularly in the blue–green region of the visible spectrum, and a comprehensive study considering the NIR PL characteristics has not been conducted yet.

Herein, we report the existence of NIR emissive states in the carbon cores of CDs, which are completely independent from their visible-light emissive surface states. This was performed by directly manipulating their surface structures. Subsequently, the optical properties of the CDs before and after the manipulation were evaluated by linear absorption, time-resolved PL, and femtosecond transient absorption (TA) spectroscopies, and the properties were then correlated to the structural changes. Combining the results of these experiments with an *ab initio* analysis, we demonstrate that the visible and NIR PL have different chemical origins and propose that small (1–2 nm) graphitic subregions in the CDs generate the NIR emissive states. The validity of the proposed mechanism was further verified by a comparative analysis with graphene oxide and other types of CDs obtained by different synthetic methods. Finally, we propose a comprehensive energy structure for the observed emissions.

2. Materials and methods

2.1. Synthesis of the CDs

To synthesize the CDs, 100 mg of graphite powder (<20 μm, Sigma-Aldrich, Korea) was added to 20 mL of the acid mixture (sulfuric acid:nitric acid = 3:1) and sonicated for 30 min. The mixture was then refluxed at 100 °C for 24 h. After cooling to room temperature, the solution was added to 100 mL of water and vacuum-filtered using filter paper to remove the solid residue. The filtrate was dialyzed against 2 L of deionized (DI) water for 7 days (with the DI water replaced every 24 h) using Spectra/Por Biotech Cellulose Ester dialysis tubes (3.5–5 kg/mol). After lyophilization of the solution, the resulting powder was stored in a freezer for further use.

2.2. Deprotonation of the CDs

To prepare the d-CDs, 1 mL of Na_2S (2.5 M) aqueous solution was added to 0.5 mL of the CD (5 mg/mL) aqueous solution in a vial. The color of the solution immediately changed from brown to black, indicating that the CDs were deprotonated.

2.3. Characterization

Transmission electron microscopy (TEM) was performed using a JEM-2200FS instrument (JEOL) equipped with a Cs corrector. Raman Spectroscopy was performed by using a XperRam S spectrometer with a 2 mW laser excitation wavelength of 532 nm. X-ray powder diffraction (XRD) patterns were recorded by an X-ray diffractometer (D8 Advance (TRIO/TWIN), Bruker) using a Cu Kα radiation at 40 kV and 40 mA and scan rate of 6°/min in the range of 5°–80° with a silicon holder. X-ray photoelectron spectroscopy (XPS) was conducted using an Escalab 250 spectrometer with an Al X-ray source (1486.6 eV). Fourier-transform infrared spectroscopy (FTIR) were recorded on a Nicolet iS50 FTIR spectrometer. UV–VIS absorption and visible PL spectroscopies were performed using 10 mm × 10 mm QS-grade quartz cuvettes (Hellma Analytics 111-QS). Light absorption spectra were recorded on a Scinco S-3100 spectrophotometer, and the PL spectra were recorded on a Jasco FP-8500 fluorometer. The quantum yields were measured using 2 mm × 10 mm QS-grade quartz cuvettes (Jasco Parts Center 6808-H250A). NIR PL spectroscopy was performed using a HORIBA PTI QM-500 spectrometer with a conventional diode laser as the light source (660 nm, 1 W). In the TA spectroscopy setup, a Ti:sapphire amplifier was used as the fundamental light source with a 1-kHz repetition rate and 80-fs pulse duration (Libra, Coherent, USA), and the beam was divided in half using a beam splitter. Approximately 95% of the light was used for the optical parametric amplifier (TOPAS Prime, Light Conversion, Lithuania), which was used as a pump pulse. The pump (excitation) beam was tuned to 350, 480, or 520 nm with an intensity of 1 μJ/pulse for each wavelength. The remaining 5% of the fundamental light was focused on a nonlinear crystal and provided a white-light-continuum broadband probe pulse in the visible spectral range of 450–780 nm. The broadband probe pulse was used to detect changes in absorption in the frequency domain as a function of the delay time between the pump and probe pulses. To avoid trap filling and second-order charge recombination, a weak probe pulse was necessary. Femtosecond TA data were acquired using a commercial TA spectrometer with a 1024-pixel CCD sensor (Helios, Ultrafast Systems, USA). The PL lifetime was measured using a FluoTime 300 spectrometer. The samples were excited with a 405-nm excitation wavelength using a picosecond-pulse laser head (LDH-P-C-405B, PicoQuant), and their lifetimes were measured using a photon counting detector (PMA Hybrid 07) with a time-correlated single photon counting (TCSPC) module (PicoHarp, PicoQuant). For the computational analysis, all calculations were performed using the DMol^3 suite of codes on a standard personal computer. BIOVIA Materials Studio 7 was used for visualization. Density functional theory (DFT) calculations were performed using the 4.4 DNP basis set.

3. Results and discussion

3.1. Surface structural modification of CDs

We chose CDs obtained by a conventional top-down approach using graphite for the analysis because they reportedly have both visible and NIR PL characteristics and negligible amounts of fluorescent byproducts are produced during their synthesis [37,41]. The chemical structure of the CDs is illustrated in Fig. 1a. Fig. 1b shows the TEM images of the ~5 nm-sized the CDs with a uniform size distribution (see Fig. S1 for more images). Using high-resolution TEM (HR-TEM) (inset of Fig. 1b), we concluded that the CDs contain distinct 1–2-nm-sized graphitic subregions embedded in an amorphous core. The Raman spectrum exhibits clear D (1350 cm^{-1}) and G (1580 cm^{-1}) bands that are typical of graphitic carbon with defects (Fig. S2). In the XRD pattern (Fig. S3), a small shoulder peak appears at $2\theta = 25°$, which is the characteristic peak of amorphous carbon. To analyze the surface chemistry of CDs, XPS and elemental analysis were conducted (Fig. S4 and Table S1). The deconvoluted C1s XPS spectra show C–C/C=C (284.7 eV), C–O (285.8 eV), C=O (287.4 eV), and O–C=O (289.7 eV) peaks, indicating the presence of hydroxyl, carbonyl, and carboxyl groups (Fig. S4b). Furthermore, the deconvoluted N1s and O1s XPS spectra show C–N–H (400.5 eV), C–N (401.9 eV), C–O (532 eV), and C–O–H (533.2 eV) peaks, which confirms the presence of oxygen and nitrogen-based defects (Figs. S4c and d). The elemental analysis data (Table S1) indicate that our CDs have very high oxygen content (45.62%) comparable to carbon content (42.3%), which can be attributed to the presence of numerous oxygen-containing defects and surface functional groups.

To change the surface chemistry, the CDs were deprotonated as

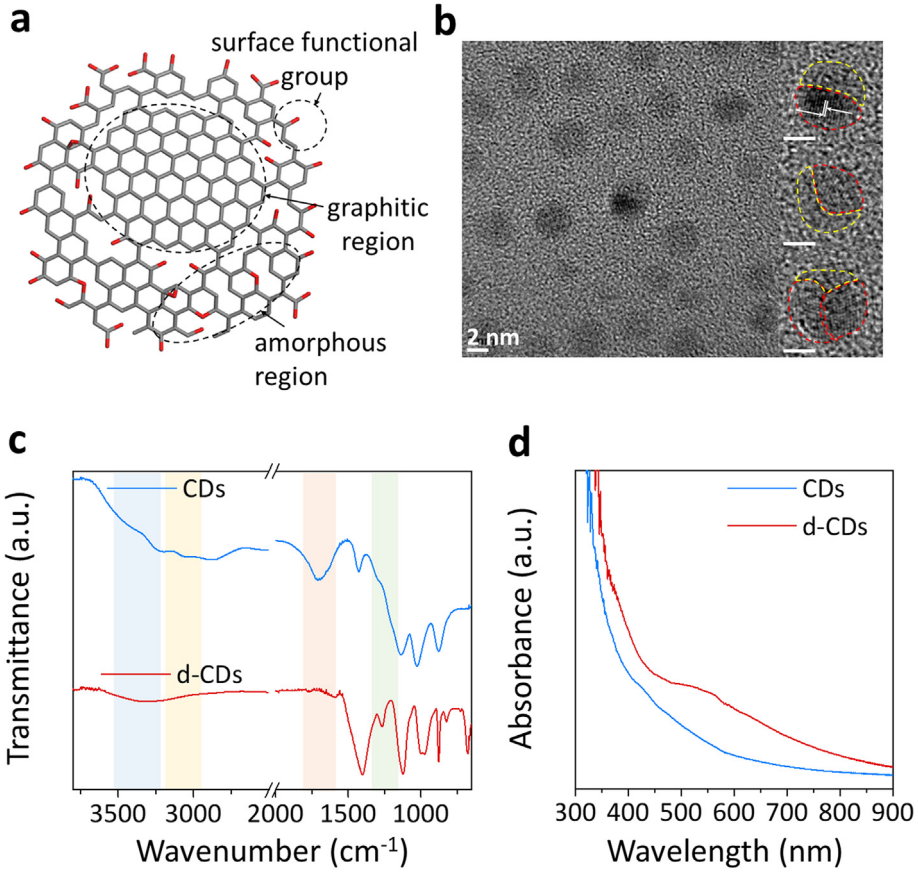

Fig. 1. (a) Illustration of the CDs. (b) TEM image of the CDs. The scale bars represent 2 nm each. Insets are HR-TEM images of the CDs. The white-solid lines and arrows denote the lattice plane distance. The dashed red and yellow circles denote the graphitic and amorphous (or oxygenic) carbon regions, respectively. (c) FTIR spectra of the CDs and d-CDs. (d) UV–VIS absorption spectra of the CDs and d-CDs. (A colour version of this figure can be viewed online.)

a way of moderate and reversible manipulation of the surface functional groups without changing the core structure. Sodium sulfide, which is a strong Lewis base, was employed to prepare the deprotonated CDs (d-CDs). The FTIR spectra (Fig. 1c) show that the carboxyl O–H (2900–3150 cm^{-1}), C=O (1730 cm^{-1}), and C–O (1210 cm^{-1}) stretching peaks disappeared, and an asymmetric C–O–O^- stretching peak (1600 cm^{-1}) appeared, indicating the deprotonation of the surface carboxylic acid and the formation of carboxylate ions. The decrease in the intensity of the hydroxyl O–H stretching peak (3200–3400 cm^{-1}) signified partial deprotonation of the surface hydroxyl groups.

The optical properties of CDs are closely related to their surface chemistry. Specifically, numerous surface functional groups produce localized energy states near the surface (so-called the surface states) of CDs, which are closely related to their optical properties. The UV–VIS absorption spectra (Figs. 1d and S5) show an overall increase in absorption in the wavelength range of 300–800 nm for the d-CDs, indicating an increase in defect states and/or noncollinear π-plasmon absorption caused by deprotonation [42,43]. In addition, the appearance of a new absorption shoulder at 550 nm indicates the generation of new energy states by deprotonation.

3.2. Contrasting changes in the visible and NIR PL upon deprotonation

The PL characteristics of the CDs and d-CDs were measured and compared to identify the relationship between the PL characteristics and surface structural changes. In Fig. 2a, the visible PL emission map of the CDs shows two excitation peaks at 350 and 480 nm associated with the broad PL emission band centered at 540 nm. Fig. S6a shows the excitation-dependent PL, considered as a unique property of CDs, indicating that the CDs have energetically different trap states induced by chemically different surface functional groups attached to the carbon core [44].

After deprotonation, the visible PL emission maps show that the original emission peak at 530 nm vanishes, and a red-shifted emission peak appears at 625 nm for the excitation wavelengths of 330 and 550 nm, indicating that deprotonation induces the development of a new excited state (Figs. 2b and S6b). This also indicates that the oxygen-containing surface functional groups, particularly those composed of functional groups that can be deprotonated in this condition, are responsible for the visible PL.

To identify the acidic surface functional groups, the changes in PL caused by deprotonation were investigated in standard buffer solutions with various pH values (Fig. S7). Because the visible emission peak the CDs remains unchanged in pH 2–11, but it is significantly shifted at pH > 12, the –OH group (pK_a 10–11) is probably the source of the visible PL, and the $-O^-$ group can induce a red shift of the emission owing to a stronger auxochromic effect. In addition, a weak excitation-independent emission peak was observed at 415 nm, which originated from the higher excited state [45]; the peak is presumably related to the amorphous core resulting from distorted C–O bonds, sp^3-bonded carbon, and/or fractions of C=C bonds in an amorphous carbon network (see Fig. S8 for the detailed analysis) [14,46,47]. It is also noteworthy that the relative PL intensity was generally decreased with

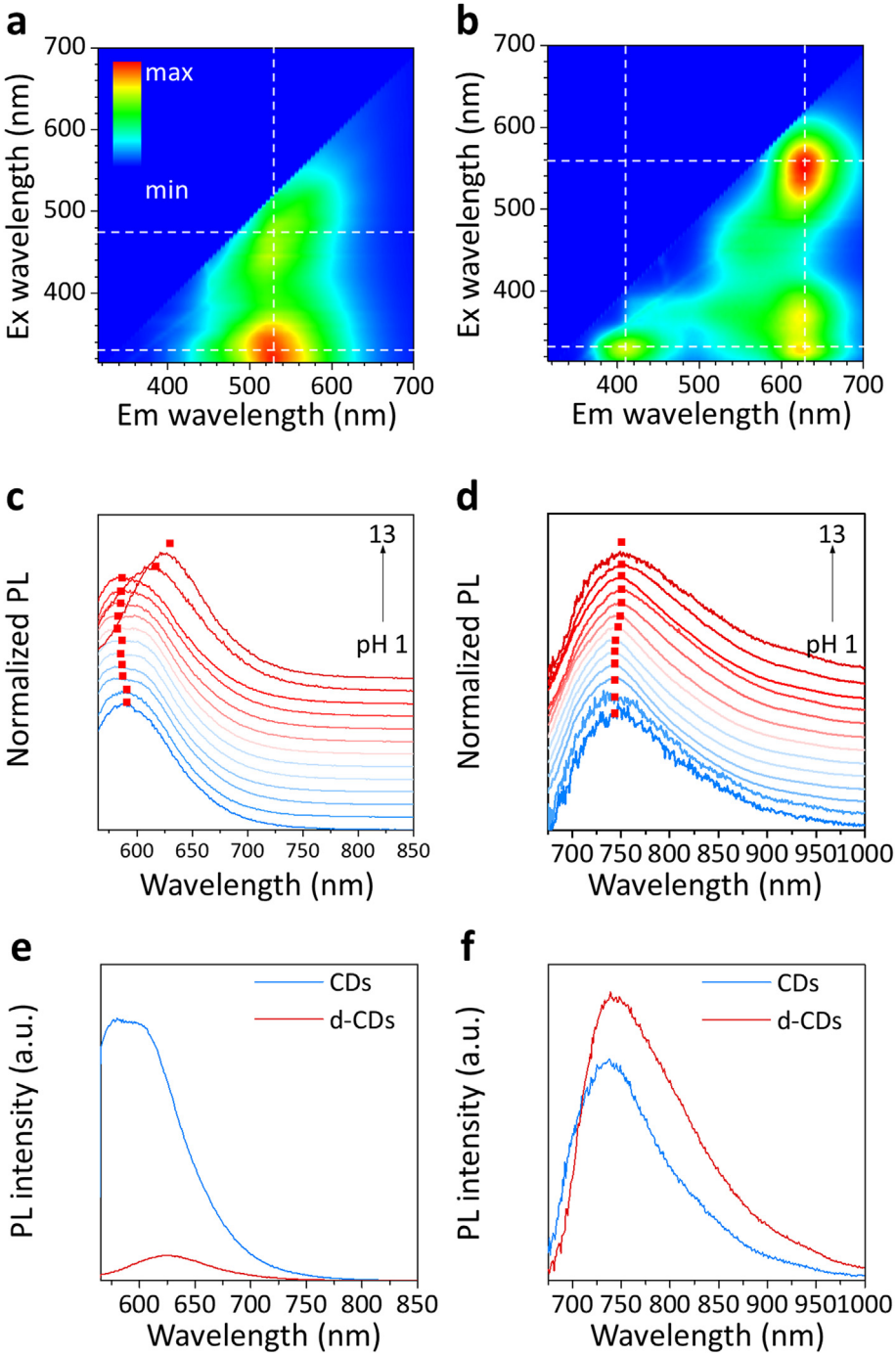

Fig. 2. (a,b) Visible PL emission map of the (a) CDs and (b) d-CDs. The dashed lines denote the emission peak wavelengths. (c,d) Normalized (c) visible and (d) NIR PL emission spectra of the CDs as a function of the solution pH. The excitation wavelengths are 550 and 660 nm, respectively, and the red square-dots demarcate the emission peaks. (e) Visible PL emission spectra of the CDs and d-CDs after excitation (at 500 and 550 nm, respectively). (f) NIR PL emission spectra of the CDs and d-CDs under 660-nm laser excitation. (A colour version of this figure can be viewed online.)

increasing pH, which can be presumably attributed to the aggregation of the CDs induced by surface charge neutralization such as protonation/deprotonation of the COOH groups [48,49].

Recently, several studies have reported that some CDs are capable of emitting NIR light [37]. In agreement with these studies, we also observed a broad NIR PL peak at 750 nm under 660 nm laser excitation (Fig. S9). Interestingly, while the visible PL changed significantly with deprotonation, the corresponding change in the NIR PL was completely different from it. To analyze the emission peak wavelength, the visible and NIR PL emission spectra of the CDs were plotted as a function of the solution pH (indicating deprotonation rate), respectively (Fig. 2c and d). By increasing the deprotonation rate, the visible emission peak wavelength of the CDs shifted drastically at pH > 12, whereas the NIR PL peak wavelength was only slightly red-shifted (~5 nm), indicating that the NIR emissive state was not strongly associated with the deprotonated surface functional groups. Additionally, the intensity of the NIR PL was enhanced via deprotonation, whereas the intensity of the

visible PL of the d-CDs decreased (Fig. 2e and f). This trend was also observed using other bases (NaOH and KOH) as deprotonation agents (Figs. S10a and b). In addition, the spectral shifts made in visible and NIR PL by deprotonation was totally reversible, which was confirmed by the neutralization experiments using acid (Figs. S10c and d). These contrasting behaviors of visible and NIR PL suggest that the NIR emissive state has a different origin from the visible emissive states, and it is rarely affected by the surface structure changes.

3.3. NIR PL due to direct recombination of photoexcited state

Femtosecond TA spectroscopy was performed to further analyze the difference in the transient carrier dynamics between NIR emission and visible emission [50]. The temporal evolution of the photoexcited carriers in the CDs and d-CDs in the direction of equilibrium was tracked by TA spectroscopy at different pump wavelengths. The pump wavelengths were chosen close to the wavelength corresponding to the energy of the deep conduction band (350 nm) and the visible excitation peak (480 and 520 nm for the CDs and d-CDs, respectively) for each sample. Fig. 3a–d shows the TA contour maps of the CDs and d-CDs, which were monitored over the 450–780 nm wavelength range (related TA spectra are shown in Figs. S11a–d). As shown in Fig. 3a and S11a, a broad photoinduced absorption (PIA) band centered at 650 nm is clearly visible for the CDs in the entire probe-energy range, and the width of the band monotonically decreases with a time delay. This indicates the absorption of carriers trapped at the oxygen-related energy sublevels, leading to an increase in the population of trap states [51–53]. After deprotonation of the CDs (Figs. 3b and S11b), the overall PIA band of the d-CDs widened at a longer probe wavelength compared to that of the CDs, which might be consistent with the red shift of the visible PL. Meanwhile, compared to the pump wavelength of 350 nm (Fig. 3a and b), the spectral shapes of the PIA band for the pump wavelengths of both 480 and 520 nm (Fig. 3c and d) changed and the spectral range of the PIA band for

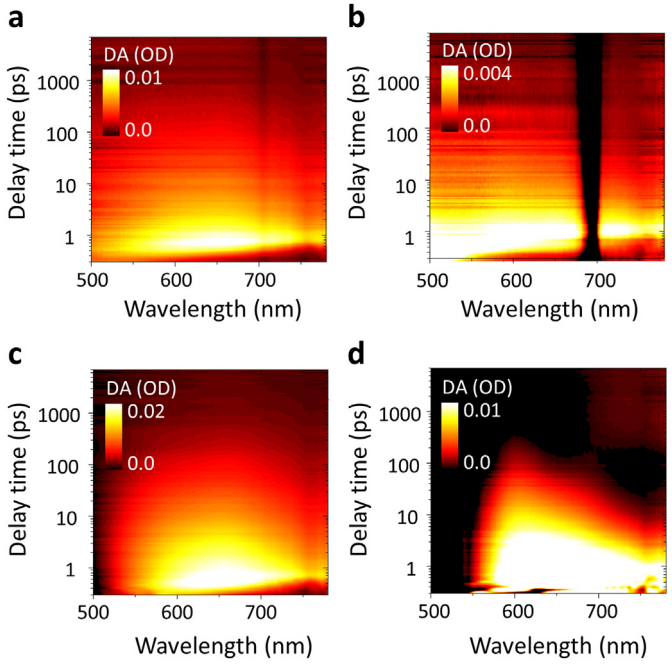

Fig. 3. TA contour maps of the (a, c) CDs and (b, d) d-CDs at excitation wavelengths of (a, b) 350 nm, (c) 480 nm, and (d) 520 nm. (A colour version of this figure can be viewed online.)

both cases shrank. By changing the pump photon energy, the excited electrons can reach around the energy of the amorphous core states (deep conduction band) after pump excitation at 350 nm, and around the energy of the surface states (band edge) after pump excitation at 480 and 520 nm (see Fig. S12 for the detailed analysis).

The ground-state photobleaching (PB) signal of probe photons is generally perceptible because of state filling and is independent of the excitation wavelength. However, PB signal was absent for both the CDs and d-CDs in the visible range, which reveals that the radiative recombination process in the visible range occurs at trap states where the excited carriers are transferred (trap emission). Considering that the surface −OH group is strongly related to the emission wavelength of the visible PL, we conclude that visible PL occurs at the oxygen-related surface states associated with the surface −OH groups.

On the other hand, a slight dip at 750 nm was observed for both the CDs and d-CDs in the NIR range, which implies the superimposition of the PB signal with the strong PIA signal. Compared to Figs. S11a and b, Figs. S11c and d show a more pronounced dip, owing to the fact that the number of accessible excited states or trap states can be decreased by using longer pump wavelengths. In Figs. S11d and a clear PB signal ($\Delta A < 0$) is observed at 750 nm after a few tens of ps time delay; this dip confirms that the PB signal is due to state filling of the photoexcited graphitic state, which has an energy gap corresponding to a wavelength of 750 nm (~1.65 eV). The state can be populated via photoexcited charge transfer from amorphous state. Considering that this wavelength is consistent with the wavelength of the NIR PL, it is inferred that the NIR PL is caused by the direct recombination of the photoexcited state and not due to the carrier trapping process.

3.4. Inhibition of the carrier trapping process by deprotonation

To track the carrier dynamics more clearly, the TA decay kinetics and for the CDs and d-CDs were monitored. First, for the visible range carrier dynamics, the decay kinetics were monitored at photon wavelengths of 540 nm (CDs) and 640 nm (d-CDs), corresponding to their visible emission peaks (excitation wavelength = 350 nm, Fig. 4a and Table 1). A global kinetics analysis was performed for each sample. The result indicated that the decay kinetics of the CDs (open blue squares in Fig. 4a) are tri-exponential with time constants of $\tau_1 = 0.85 \pm 0.1$ ps (56%), $\tau_2 = 13.8 \pm 3$ ps (27%), and $\tau_3 = 246 \pm 82$ ps (17%). The fastest component contributed 56% to the relaxation process. Because the carrier–carrier scattering in the carbon core is completed within the pulse duration (~200 fs), it is concluded that the subsequent relaxation processes take place during this time, corresponding to the trapping/de-trapping process occurring in the oxygen-related surface state. The decay component with a time constant of 13.8 ps contributes approximately 27% to relaxation under deep trap states. The slowest decay component is interpreted as a non-radiative electron-hole recombination from the surface trap states to the ground state.

After deprotonation, the decay kinetics of the d-CDs (open-red circles) show tri-exponential relaxation with three time constants, $\tau_1 = 1.15 \pm 0.1$ (62%), $\tau_2 = 20.2 \pm 3.3$ (28%), and $\tau_3 = 716 \pm 238$ ps (10%). Interestingly, all time constants are increased in the d-CDs, which implies that the carrier trapping and nonradiative recombination processes are slowed down by deprotonation. Slowing the nonradiative recombination process generally improves PL quantum yield (QY), but in the case of the d-CD, the visible PL QY is significantly decreased (Fig. S13). This may be due to the slowing of the carrier trapping process from the carbon core to the oxygen-related surface state. One plausible explanation for this is that the

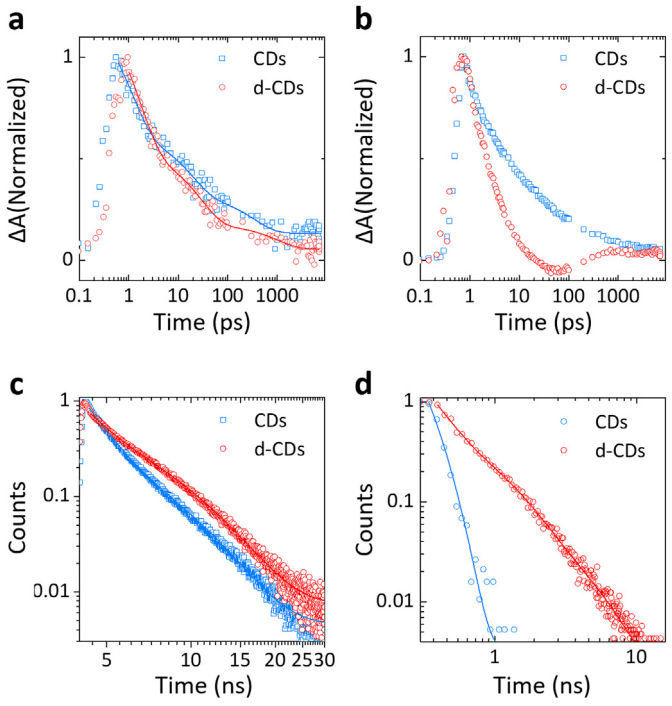

Fig. 4. (a) TA kinetics of the CDs and d-CDs at probe wavelengths of 540 and 640 nm, respectively (pump wavelength = 350 nm). (b) TA kinetics of the CDs and d-CDs at a probe wavelength of 740 nm (pump wavelength = 480 and 520 nm, respectively). (c) TCSPC kinetics of the CDs and d-CDs at probe wavelengths of 570 and 630 nm, respectively (excitation wavelength = 405 nm). (d) TCSPC kinetics of the CDs and d-CDs at a probe wavelength of 730 nm (excitation wavelength = 350 nm). (A colour version of this figure can be viewed online.)

electrons in the deprotonated oxygen-containing surface functional groups such as COO^- and O^- form repulsive potentials. Such a repulsive potential increases the energy required for additional electrons to be trapped in the surface states [54]. In general, electron trapping is the primary process for visible PL; thus, this repulsive potential could decrease the probability of trap emission and decrease the visible PL QY of the CDs.

On the other hand, the lagging electron trapping process suggests that the contribution of hot carrier relaxation in the carbon core might be increased because the untrapped electrons tend to undergo direct relaxation in the carbon core. The increased photothermal effect observed in the d-CDs may support this suggestion, because the increased hot carrier relaxation in graphitic carbon may be the main reason for the rise in temperature observed in the presence of laser irradiation (Fig. S14) [55].

3.5. Location of the NIR emissive state

To investigate the transient behavior in the NIR range, the decay kinetics of PIA at a detection photon wavelength of 750 nm, corresponding to the NIR emissive state energy, were also monitored. As shown in Fig. 4b, a PB signal (ΔA<0) appears for short delay times within the NIR range (750 nm) in the d-CDs at a photon excitation energy of 520 nm, suggesting that carrier trapping is not significant within this range and that the NIR PL is due to the direct recombination of the photoexcited state. The PB within the NIR range and changes to PIA at a greater delay time, indicating that the trap states were rapidly filled. The bleaching signal was much less pronounced and only exhibited a slight dip in the CDs at an excitation wavelength of 480 nm, owing to the strong PIA signal from the oxygen-related surface states. Considering that deprotonation inhibits the surface trapping process and increases the probability of carrier relaxation in the carbon core, the increase in the PB signal and the enhancement of the NIR PL intensity for the d-CDs suggest that the NIR emissive state is located in the carbon core.

3.6. Fluorescence lifetime analysis and energy structure model for visible and NIR PL

To further investigate the dynamics of radiative recombination, time-correlated single photon counting (TCSPC) measurements were conducted. Fig. 4c shows the TCSPC signals of the CDs and d-CDs recorded at their respective visible PL peaks at an excitation wavelength of 405 nm. All the signals were fitted using a double-exponential decay model. As shown in Table 2, the average lifetime of the d-CDs (3.94 ns) was nearly the same as that of the CDs (3.31 ns) despite the significant decrease in the visible PL QY of the CDs. The TCSPC signals were also recorded at the NIR PL peaks at an excitation wavelength of 350 nm (Fig. 4d). The average lifetime of the d-CDs (0.14 ns) was doubled compared to that of the CDs (0.07 ns), which is consistent with the increased NIR PL intensity.

For a detailed analysis, a simplified energy structure model was constructed, as shown in Fig. S15. In the energy structure model of the CDs with core and surface trap states, the fluorescence lifetime of each state is expressed by the following equations:

$$\tau_{core} = \frac{1}{k_{r,core} + k_{nr,core} + k_{CT}} \quad (1)$$

$$\tau_{surf} = \frac{1}{k_{r,surf} + k_{nr,surf}} \quad (2)$$

$$\Phi_{core} = \frac{k_{r,core}}{k_{r,core} + k_{nr,core} + k_{CT}} \quad (3)$$

$$\Phi_{surf} = \frac{k_{CT}}{k_{r,core} + k_{nr,core} + k_{CT}} \times \frac{k_{r,surf}}{k_{r,surf} + k_{nr,surf}} \quad (4)$$

where τ and Φ are the fluorescence lifetime and fluorescence QY of the sample, respectively, and k_r, k_{nr}, and k_{CT} are the rate constants of fluorescence, nonradiative decay, and carrier transfer (electron trapping), respectively. The subscripts *surf* and *core* denote the energy state (surface state or core state) that is associated with the corresponding parameters.

According to equations (2) and (4), the fluorescence QY of the surface state emission is related to the rate of carrier transfer, but the fluorescence lifetime is not. This is consistent with the TCSPC results that the visible PL lifetime was unchanged despite the significant decrease in the visible PL intensity due to inhibition of the carrier transfer process. However, the fluorescence lifetime and

Table 1
Decay components obtained via TA of the CDs and d-CDs.

Sample	Pump wavelength (nm)	Probe wavelength (nm)	τ_1 (ps)	τ_2 (ps)	τ_3 (ps)
CDs	350	540	0.85 (56%)	13.8 (27%)	246 (17%)
d-CDs	350	640	1.15 (62%)	20.2 (28%)	716 (10%)

Table 2
Visible and NIR PL lifetimes of the CDs and d-CDs.

Sample	Pump probe (nm)	Detect probe (nm)	t_1 (ns)	a_1	t_2 (ns)	a_2	t_3 (ns)	a_3	t_{avg} (ns)
CDs	405	570	4.76	60.27	1.10	39.73	–	–	3.31
d-CDs	405	630	4.64	80.19	1.13	19.81	–	–	3.94
CDs	350	750	0.07	100	–	–	–	–	0.07
d-CDs	350	750	0.1	91.91	0.48	7.23	1.97	0.86	0.14

fluorescence QY of the core state emission are inversely proportional to the rate of carrier transfer, which could be the reason for the increased NIR PL lifetime and NIR PL intensity of the d-CDs. The scale of the NIR PL lifetime is extremely short because of the fast intrinsic fluorescence lifetime of this process and the use of a high-energy pump excitation source (350 nm), which implies that the energy of the photoexcited electron is dissipated via multiple routes.

3.7. Comparative study with graphene oxide (GO) and chemical origin of NIR PL

Based on the results of the steady-state and transient-optical characterization, we discovered that the NIR PL originates from direct recombination in the carbon core, which is completely different from the origin for the visible PL. To demonstrate which carbon core structure produces NIR PL, we introduced an energy structure model of GO into our hypothesis. The GO structure has graphitic subregions isolated from the oxidized amorphous core owing to various defects, disordered structures, and functional groups [56–60]. Localized energy states from functionalized groups and some oxidized amorphous sites contribute to the visible fluorescence in GOs, whereas unoxidized graphitic subregions (2.5–6 nm) contribute to the band structure having a bandgap of ~0.6 eV [61].

Because our CDs are synthesized via the oxidation of graphite, their structure is similar to that of GO [26,62]. Therefore, we hypothesized that the CDs have similar but smaller graphitic subregions than those of GOs owing to their particle size (~5 nm), and that the bandgap formed by the graphitic subregions in the CDs are larger than that of GO owing to a smaller π-electron delocalization. This might be the origin of the NIR PL from the CDs. According to the calculation results of Sk et al. and our DFT calculation of the emission wavelength as a function of the diameter of the graphitic subregion (Fig. 5a) [23], the energy gap of the NIR PL (750 nm) can be obtained by the π-electron delocalization in the graphitic subregion of 1.6–2.1 nm (red shade). Revisiting the TEM results in Fig. 1b, the graphitic subregion of the CDs was ca. 1.5–2 nm, which exactly matches with the calculated results and confirms the plausibility of our hypothesis.

Notably, GOs exhibit an NIR PL band that is similar to the CDs (Fig. S16). A previous study reported that the NIR PL from GOs is attributed to the π–π* transition in graphitic subregions [63]. Therefore, it is plausible that the CDs also exhibit NIR PL originating from the π–π* transition in the small graphitic subregions. The peak emission wavelength of the NIR PL of the CD is blue-shifted by ~20 nm compared to that of the GOs, indicating that the average size of the small graphitic subregions in the CDs is smaller than that in the GOs. In conclusion, we propose that the NIR PL occurring at 750 nm originated from the small graphitic subregions (1–2 nm) in the carbon core.

3.8. Comprehensive electronic structure of the CDs

We have presented the proposed electronic structure of the CDs in Fig. 5b. In the carbon core, small graphitic subregions are surrounded by an oxidized amorphous core with numerous trap sites. The small graphitic subregions (1–2 nm) in the carbon core form an interband-energy gap of 1.69 eV, which produces the NIR PL (graphitic state), and the amorphous core with surface functional groups forms the energy states responsible for the visible PL. Excitons were generated in the carbon core upon absorbing light. These excitons are then trapped in the surface states formed by oxygen-containing surface functional groups (probably containing –OH groups) and generate an excitation-dependent visible PL. Deprotonation changes the surface –OH groups into $–O^-$ groups and results in a red-shifted visible PL, but no shift occurs in the NIR PL emission wavelength because its responsible energy states are embedded in the core. In addition, due to electron trapping inhibition for the surface states, the emission intensity of visible PL

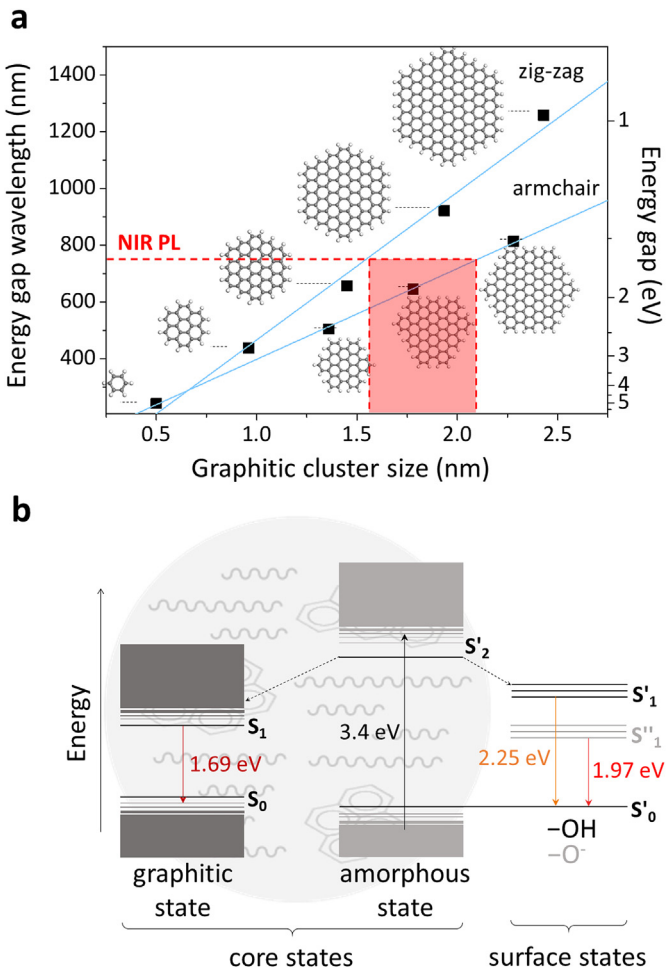

Fig. 5. (a) Simulated energy gap as a function of the size of graphitic cluster using DFT method. The solid lines are the linear fitting of zigzag-edged clusters and armchair-edged clusters. The cluster size is the average of the horizontal and vertical lengths of the graphitic clusters. (b) Proposed comprehensive energy structure for the CDs. (A colour version of this figure can be viewed online.)

decreases and that of NIR PL increases.

3.9. Comparative study with other types of CDs and the universality of the proposed model

To test the universality of our findings, we synthesized several types of CDs using various synthesis methods and precursors and measured their PL in NIR range. The preparation methods of CD1 [64], CD2 [65], CD3 [66] and CD4 [24] have been reported in previous studies. Remarkably, we observed that these CDs, even though they were known to show only visible PL, showed NIR PL under 660 nm laser excitation (Fig. S17). Furthermore, all the prepared materials exhibited almost the same NIR emission peak wavelength compared to our CD in their PL spectra, even though their visible PL peaks were different due to the variety of surface states. This implies that the graphitic state (directly responsible for NIR PL) may be universally present in various types of CDs. (Fig. S18 and Table S2). Unfortunately, the deprotonation strategy suggested in our study is hardly applicable to other types of CDs due to their different surface chemistry (see Fig. S19 for more details). Furthermore, it should be noted that the graphitic state may be not the sole origin of NIR PL because it can also occur as a result of chemical doping and surface engineering to energetically modify the original trap or surface states of CDs [67]. The transient spectroscopic features of this kind of CDs may be demonstrated by carrier trapping kinetics rather than direct recombination. Although further studies are necessary to prove the universality of this finding, this result indicates that our proposed electronic structure can be applied to a variety of CDs.

4. Conclusion

In conclusion, we discovered the existence of NIR emissive states originating from the graphitic core of the CDs using the following strategies. First, modulation of the surface structure using deprotonation helped to confirm that the visible emissions were only owing to the surface states. Second, it was discovered that the NIR emissive states were independent of the surface states. Third, transient analysis for the CDs and d-CDs showed that the NIR emissive state and visible emissive state had different carrier dynamics. Finally, combined with the DFT calculation results, it is proposed that the NIR emission of the CDs originates from the direct recombination of carriers in small (1–2 nm) graphitic subregions and not from carrier trapping that is responsible for visible emission. Regarding the universality of the proposed NIR PL mechanism, our findings are not confined to our CDs but can provide a new insight into the role of the carbon core in conventional CDs. Finally, we expect that the demonstrated new energy structure model may pave the way for a better understanding of the optical behavior of CDs and expand their potential as a NIR imaging contrast.

CRediT authorship contribution statement

Yoonsang Park: Methodology, Investigation, synthesis & chemical, Formal analysis, Writing – original draft. **Minh Dao Tran:** Methodology, Investigation, ultrafast spectroscopy, Writing – original draft. **Yujin Kim:** Investigation, Validation, Formal analysis. **Sungyeon Won:** Investigation, Formal analysis. **Young-Hoon Kim:** Investigation, spectroscopy. **Tae-Woo Lee:** Resources, spectroscopy. **Tom Gregorkiewicz:** Writing – review & editing. **Young Hee Lee:** Writing – review & editing, Resources. **Ji-Hee Kim:** Writing – review & editing, Supervision, ultrafast spectroscopy. **Woosung Kwon:** Writing – review & editing, Supervision, Project administration.

Declaration of competing interest

The authors declare that they have no known competing financial interests or personal relationships that could have appeared to influence the work reported in this paper.

Acknowledgements

This work was supported by the Basic Science Research Program (NRF-2019R1C1C1006574) of the National Research Foundation of Korea. Y.H.L and J.-H.K acknowledge financial support from the Institute for Basic Science of Korea (IBS-R011-D1). Y.P. and W.K. thank Sung In Kim (KANC) for her assistance with transmission electron microscopy.

Appendix A. Supplementary data

Supplementary data to this article can be found online at https://doi.org/10.1016/j.carbon.2021.11.063.

References

[1] Y.-P. Sun, B. Zhou, Y. Lin, W. Wang, K.A.S. Fernando, P. Pathak, M.J. Meziani, B.A. Harruff, X. Wang, H. Wang, P.G. Luo, H. Yang, M.E. Kose, B. Chen, L.M. Veca, S.-Y. Xie, Quantum-sized carbon dots for bright and colorful photoluminescence, J. Am. Chem. Soc. 128 (24) (2006) 7756–7757.
[2] A. Zhao, Z. Chen, C. Zhao, N. Gao, J. Ren, X. Qu, Recent advances in bioapplications of C-dots, Carbon 85 (2015) 309–327.
[3] X.T. Zheng, A. Ananthanarayanan, K.Q. Luo, P. Chen, Glowing graphene quantum dots and carbon dots: properties, syntheses, and biological applications, Small 11 (14) (2015) 1620–1636.
[4] H. Li, Z. Kang, Y. Liu, S.-T. Lee, Carbon nanodots: synthesis, properties and applications, J. Mater. Chem. 22 (46) (2012) 24230–24253.
[5] Y. Park, J. Yoo, B. Lim, W. Kwon, S.W. Rhee, Improving the functionality of carbon nanodots: doping and surface functionalization, J. Mater. Chem. A 4 (30) (2016) 11582–11603.
[6] X. Bao, Y. Yuan, J. Chen, B. Zhang, D. Li, D. Zhou, P. Jing, G. Xu, Y. Wang, K. Holá, D. Shen, C. Wu, L. Song, C. Liu, R. Zboril, S. Qu, In vivo theranostics with near-infrared-emitting carbon dots-highly efficient photothermal therapy based on passive targeting after intravenous administration, Light Sci. Appl. 7 (2018), 91-91.
[7] Q. Zhang, S. Deng, J. Liu, X. Zhong, J. He, X. Chen, B. Feng, Y. Chen, K. Ostrikov, Cancer-Targeting graphene quantum dots: fluorescence quantum yields, stability, and cell selectivity, Adv. Funct. Mater. 29 (5) (2019) 1805860.
[8] B. Zhi, Y. Cui, S. Wang, B.P. Frank, D.N. Williams, R.P. Brown, E.S. Melby, R.J. Hamers, Z. Rosenzweig, D.H. Fairbrother, G. Orr, C.L. Haynes, Malic acid carbon dots: from super-resolution live-cell imaging to highly efficient separation, ACS Nano 12 (6) (2018) 5741–5752.
[9] W. Li, S. Wu, H. Zhang, X. Zhang, J. Zhuang, C. Hu, Y. Liu, B. Lei, L. Ma, X. Wang, Enhanced biological photosynthetic efficiency using light-harvesting engineering with dual-emissive carbon dots, Adv. Funct. Mater. 28 (44) (2018) 1804004.
[10] H. Kim, Y. Park, S. Beack, S. Han, D. Jung, H.J. Cha, W. Kwon, S.K. Hahn, Dual-color-emitting carbon nanodots for multicolor bioimaging and optogenetic control of ion channels, Adv. Sci. 4 (11) (2017) 1700325.
[11] H. Nie, M. Li, Q. Li, S. Liang, Y. Tan, L. Sheng, W. Shi, S.X.-A. Zhang, Carbon dots with continuously tunable full-color emission and their application in ratiometric pH sensing, Chem. Mater. 26 (10) (2014) 3104–3112.
[12] S. Nishitani, R. Sekiya, I. Matsumoto, T. Haino, Blueish-white-light-emitting nanographenes developed by Pd-catalyzed suzuki-miyaura cross coupling reactions, Chem. Lett. 50 (4) (2021) 664–667.
[13] R. Sekiya, Y. Uemura, H. Murakami, T. Haino, White-light-emitting edge-functionalized graphene quantum dots, Angew. Chem. Int. Ed. 53 (22) (2014) 5619–5623.
[14] B. van Dam, H. Nie, B. Ju, E. Marino, J.M.J. Paulusse, P. Schall, M. Li, K. Dohnalová, Excitation-dependent photoluminescence from single-carbon dots, Small 13 (48) (2017) 1702098.
[15] E.J. Goh, K.S. Kim, Y.R. Kim, H.S. Jung, S. Beack, W.H. Kong, G. Scarcelli, S.H. Yun, S.K. Hahn, Bioimaging of hyaluronic acid derivatives using nanosized carbon dots, Biomacromolecules 13 (8) (2012) 2554–2561.
[16] W. Kwon, Y.-H. Kim, C.-L. Lee, M. Lee, H.C. Choi, T.-W. Lee, S.-W. Rhee, Electroluminescence from graphene quantum dots prepared by amidative cutting of tattered graphite, Nano Lett. 14 (3) (2014) 1306–1311.
[17] Y. Dong, R. Wang, G. Li, C. Chen, Y. Chi, G. Chen, Polyamine-functionalized carbon quantum dots as fluorescent probes for selective and sensitive detection of copper ions, Anal. Chem. 84 (14) (2012) 6220–6224.
[18] H. Choi, S.-J. Ko, Y. Choi, P. Joo, T. Kim, B.R. Lee, J.-W. Jung, H.J. Choi, M. Cha, J.-R. Jeong, I.-W. Hwang, M.H. Song, B.-S. Kim, J.Y. Kim, Versatile surface plasmon

resonance of carbon-dot-supported silver nanoparticles in polymer optoelectronic devices, Nat. Photonics 7 (9) (2013) 732–738.
[19] L. Energy, , Environmental ScienceCatalysis Surveys from AsiaCao, S. Sahu, P. Anilkumar, C.E. Bunker, J. Xu, K.A.S. Fernando, P. Wang, E.A. Guliants, K.N. Tackett, Y.-P. Sun, Carbon nanoparticles as visible-light photocatalysts for efficient CO2 conversion and beyond, J. Am. Chem. Soc. 133 (13) (2011) 4754–4757.
[20] S. Dong, Y. Song, Y. Fang, K. Zhu, K. Ye, Y. Gao, J. Yan, G. Wang, D. Cao, Microwave-assisted synthesis of carbon dots modified graphene for full carbon-based potassium ion capacitors, Carbon 178 (2021) 1–9.
[21] S. Mondal, C.P. Vinod, U.K. Gautam, 'Autophagy' and unique aerial oxygen harvesting properties exhibited by highly photocatalytic carbon quantum dots, Carbon 181 (2021) 16–27.
[22] S. Zhu, Y. Song, X. Zhao, J. Shao, J. Zhang, B. Yang, The photoluminescence mechanism in carbon dots (graphene quantum dots, carbon nanodots, and polymer dots): current state and future perspective, Nano Res 8 (2) (2015) 355–381.
[23] M.A. Sk, A. Ananthanarayanan, L. Huang, K.H. Lim, P. Chen, Revealing the tunable photoluminescence properties of graphene quantum dots, J. Mater. Chem. C 2 (34) (2014) 6954–6960.
[24] Y. Song, S. Zhu, S. Zhang, Y. Fu, L. Wang, X. Zhao, B. Yang, Investigation from chemical structure to photoluminescent mechanism: a type of carbon dots from the pyrolysis of citric acid and an amine, J. Mater. Chem. C 3 (23) (2015) 5976–5984.
[25] L. Wang, S.-J. Zhu, H.-Y. Wang, S.-N. Qu, Y.-L. Zhang, J.-H. Zhang, Q.-D. Chen, H.-L. Xu, W. Han, B. Yang, H.-B. Sun, Common origin of green luminescence in carbon nanodots and graphene quantum dots, ACS Nano 8 (3) (2014) 2541–2547.
[26] G. Eda, Y.-Y. Lin, C. Mattevi, H. Yamaguchi, H.-A. Chen, I.S. Chen, C.-W. Chen, M. Chhowalla, Blue photoluminescence from chemically derived graphene oxide, Adv. Mater. 22 (4) (2010) 505–509.
[27] J. Peng, W. Gao, B.K. Gupta, Z. Liu, R. Romero-Aburto, L. Ge, L. Song, L.B. Alemany, X. Zhan, G. Gao, S.A. Vithayathil, B.A. Kaipparettu, A.A. Marti, T. Hayashi, J.-J. Zhu, P.M. Ajayan, Graphene quantum dots derived from carbon fibers, Nano Lett. 12 (2) (2012) 844–849.
[28] L. Tang, R. Ji, X. Cao, J. Lin, H. Jiang, X. Li, K.S. Teng, C.M. Luk, S. Zeng, J. Hao, S.P. Lau, Deep ultraviolet photoluminescence of water-soluble self-passivated graphene quantum dots, ACS Nano 6 (6) (2012) 5102–5110.
[29] F. Yuan, S. Li, Z. Fan, X. Meng, L. Fan, S. Yang, Shining carbon dots: synthesis and biomedical and optoelectronic applications, Nano Today 11 (5) (2016) 565–586.
[30] X. Wang, L. Cao, S.-T. Yang, F. Lu, M.J. Meziani, L. Tian, K.W. Sun, M.A. Bloodgood, Y.-P. Sun, Bandgap-like strong fluorescence in functionalized carbon nanoparticles, Angew. Chem. Int. Ed. 49 (31) (2010) 5310–5314.
[31] H. Ding, X.-X. Zhou, J.-S. Wei, X.-B. Li, B.-T. Qin, X.-B. Chen, H.-M. Xiong, Carbon dots with red/near-infrared emissions and their intrinsic merits for biomedical applications, Carbon 167 (2020) 322–344.
[32] Y. Liu, D. Chao, L. Zhou, Y. Li, R. Deng, H. Zhang, Yellow emissive carbon dots with quantum yield up to 68.6% from manganese ions, Carbon 135 (2018) 253–259.
[33] X. Shi, H. Meng, Y. Sun, L. Qu, Y. Lin, Z. Li, D. Du, Far-red to near-infrared carbon dots: preparation and applications in biotechnology, Small 15 (48) (2019) 1901507.
[34] W. Yang, H. Zhang, J. Lai, X. Peng, Y. Hu, W. Gu, L. Ye, Carbon dots with red-shifted photoluminescence by fluorine doping for optical bio-imaging, Carbon 128 (2018) 78–85.
[35] R. Li, F. Wei, X. Wu, P. Zhou, Q. Chen, Y. Cen, G. Xu, X. Cheng, A. Zhang, Q. Hu, PEI modified orange emissive carbon dots with excitation-independent fluorescence emission for cellular imaging and siRNA delivery, Carbon 177 (2021) 403–411.
[36] S. Yi, S. Deng, X. Guo, C. Pang, J. Zeng, S. Ji, H. Liang, X.-C. Shen, B.-P. Jiang, Red emissive two-photon carbon dots: photodynamic therapy in combination with real-time dynamic monitoring for the nucleolus, Carbon 182 (2021) 155–166.
[37] H. Tao, K. Yang, Z. Ma, J. Wan, Y. Zhang, Z. Kang, Z. Liu, In vivo NIR fluorescence imaging, biodistribution, and toxicology of photoluminescent carbon dots produced from carbon nanotubes and graphite, Small 8 (2) (2012) 281–290.
[38] Y. Li, G. Bai, S. Zeng, J. Hao, Theranostic carbon dots with innovative NIR-II emission for in vivo renal-excreted optical imaging and photothermal therapy, ACS Appl. Mater. Interfaces 11 (5) (2019) 4737–4744.
[39] L. Tang, R. Ji, X. Li, G. Bai, C.P. Liu, J. Hao, J. Lin, H. Jiang, K.S. Teng, Z. Yang, S.P. Lau, Deep ultraviolet to near-infrared emission and photoresponse in layered N-doped graphene quantum dots, ACS Nano 8 (6) (2014) 6312–6320.
[40] E. Liu, T. Liang, E.V. Ushakova, B. Wang, B. Zhang, H. Zhou, G. Xing, C. Wang, Z. Tang, S. Qu, A.L. Rogach, Enhanced near-infrared emission from carbon dots by surface deprotonation, J. Phys. Chem. Lett. 12 (1) (2021) 604–611.
[41] J.B. Essner, J.A. Kist, L. Polo-Parada, G.A. Baker, Artifacts and errors associated with the ubiquitous presence of fluorescent impurities in carbon nanodots, Chem. Mater. 30 (6) (2018) 1878–1887.
[42] P. Johari, V.B. Shenoy, Modulating optical properties of graphene oxide: role of prominent functional groups, ACS Nano 5 (9) (2011) 7640–7647.
[43] T. Pichler, M. Knupfer, M.S. Golden, J. Fink, A. Rinzler, R.E. Smalley, Localized and delocalized electronic states in single-wall carbon nanotubes, Phys. Rev. Lett. 80 (21) (1998) 4729–4732.
[44] A. Sharma, T. Gadly, A. Gupta, A. Ballal, S.K. Ghosh, M. Kumbhakar, Origin of excitation dependent fluorescence in carbon nanodots, J. Phys. Chem. Lett. 7 (18) (2016) 3695–3702.
[45] T. Itoh, Fluorescence and phosphorescence from higher excited states of organic molecules, Chem. Rev. 112 (8) (2012) 4541–4568.
[46] J.T. Margraf, V. Strauss, D.M. Guldi, T. Clark, The electronic structure of amorphous carbon nanodots, J. Phys. Chem. B 119 (24) (2015) 7258–7265.
[47] C. Mathioudakis, G. Kopidakis, P.C. Kelires, P. Patsalas, M. Gioti, S. Logothetidis, Electronic and optical properties of a-C from tight-binding molecular dynamics simulations, Thin Solid Films 482 (1) (2005) 151–155.
[48] X. Jia, J. Li, E. Wang, One-pot green synthesis of optically pH-sensitive carbon dots with upconversion luminescence, Nanoscale 4 (18) (2012) 5572–5575.
[49] H. Ehtesabi, Z. Hallaji, S. Najafi Nobar, Z. Bagheri, Carbon dots with pH-responsive fluorescence: a review on synthesis and cell biological applications, Microchim. Acta 187 (2) (2020) 150.
[50] R. Berera, R. van Grondelle, J.T.M. Kennis, Ultrafast transient absorption spectroscopy: principles and application to photosynthetic systems, Photosynth. Res. 101 (2) (2009) 105–118.
[51] L. Wang, H.-Y. Wang, Y. Wang, S.-J. Zhu, Y.-L. Zhang, J.-H. Zhang, Q.-D. Chen, W. Han, H.-L. Xu, B. Yang, H.-B. Sun, Direct observation of quantum-confined graphene-like states and novel Hybrid states in graphene oxide by transient spectroscopy, Adv. Mater. 25 (45) (2013) 6539–6545.
[52] S. Kaniyankandy, S.N. Achary, S. Rawalekar, H.N. Ghosh, Ultrafast relaxation dynamics in graphene oxide: evidence of electron trapping, J. Phys. Chem. C 115 (39) (2011) 19110–19116.
[53] V. Strauss, J.T. Margraf, C. Dolle, B. Butz, T.J. Nacken, J. Walter, W. Bauer, W. Peukert, E. Spiecker, T. Clark, D.M. Guldi, Carbon nanodots: toward a comprehensive understanding of their photoluminescence, J. Am. Chem. Soc. 136 (49) (2014) 17308–17316.
[54] D.B. Tice, M.T. Frederick, R.P.H. Chang, E.A. Weiss, Electron migration limits the rate of photobrightening in thin films of CdSe quantum dots in a dry N2 (g) atmosphere, J. Phys. Chem. C 115 (9) (2011) 3654–3662.
[55] G.M. Neelgund, A. Oki, Photothermal effect: an important aspect for the enhancement of photocatalytic activity under illumination by NIR radiation, Mater. Chem. Front. 2 (1) (2018) 64–75.
[56] Z.-B. Liu, X. Zhao, X.-L. Zhang, X.-Q. Yan, Y.-P. Wu, Y.-S. Chen, J.-G. Tian, Ultrafast dynamics and nonlinear optical responses from sp2- and sp3-hybridized domains in graphene oxide, J. Phys. Chem. Lett. 2 (16) (2011) 1972–1977.
[57] G. Eda, M. Chhowalla, Chemically derived graphene oxide: towards large-area thin-film electronics and optoelectronics, Adv. Mater. 22 (22) (2010) 2392–2415.
[58] K.P. Loh, Q. Bao, G. Eda, M. Chhowalla, Graphene oxide as a chemically tunable platform for optical applications, Nat. Chem. 2 (12) (2010) 1015–1024.
[59] K. Erickson, R. Erni, Z. Lee, N. Alem, W. Gannett, A. Zettl, Determination of the local chemical structure of graphene oxide and reduced graphene oxide, Adv. Mater. 22 (40) (2010) 4467–4472.
[60] S. Saxena, T.A. Tyson, E. Negusse, Investigation of the local structure of graphene oxide, J. Phys. Chem. Lett. 1 (24) (2010) 3433–3437.
[61] J. Shang, L. Ma, J. Li, W. Ai, T. Yu, G.G. Gurzadyan, The origin of fluorescence from graphene oxide, Sci. Rep. 2 (2012), 792-792.
[62] S. Zhu, Q. Meng, L. Wang, J. Zhang, Y. Song, H. Jin, K. Zhang, H. Sun, H. Wang, B. Yang, Highly photoluminescent carbon dots for multicolor patterning, sensors, and bioimaging, Angew. Chem. Int. Ed. 52 (14) (2013) 3953–3957.
[63] X.-F. Zhang, X. Shao, S. Liu, Dual fluorescence of graphene oxide: a time-resolved study, J. Phys. Chem. A 116 (27) (2012) 7308–7313.
[64] W. Kwon, G. Lee, S. Do, T. Joo, S.-W. Rhee, Size-controlled soft-template synthesis of carbon nanodots toward versatile photoactive materials, Small 10 (3) (2014) 506–513.
[65] C. Lee, W. Kwon, S. Beack, D. Lee, Y. Park, H. Kim, S.K. Hahn, S.-W. Rhee, C. Kim, Biodegradable nitrogen-doped carbon nanodots for non-invasive photoacoustic imaging and photothermal therapy, Theranostics 6 (12) (2016) 2196–2208.
[66] X. Dong, Y. Su, H. Geng, Z. Li, C. Yang, X. Li, Y. Zhang, Fast one-step synthesis of N-doped carbon dots by pyrolyzing ethanolamine, J. Mater. Chem. C 2 (36) (2014) 7477–7481.
[67] D. Li, P. Jing, L. Sun, Y. An, X. Shan, X. Lu, D. Zhou, D. Han, D. Shen, Y. Zhai, S. Qu, R. Zbořil, A.L. Rogach, Near-infrared excitation/emission and multiphoton-induced fluorescence of carbon dots, Adv. Mater. 30 (13) (2018) 1705913.